



Trans. Nonferrous Met. Soc. China 31(2021) 1951-1968

Transactions of Nonferrous Metals Society of China

www.tnmsc.cn



Effect of Al addition on microstructure and mechanical properties of Mg–Zn–Sn–Mn alloy

Cai-hong HOU^{1,2}, Zhi-song YE^{1,2}, Fu-gang QI^{1,2}, Qing WANG³, Lian-hui LI^{1,2}, Xiao-ping OUYANG^{1,2}, Nie ZHAO^{1,2}

- 1. School of Materials Science and Engineering, Xiangtan University, Xiangtan 411105, China;
- 2. Key Laboratory of Low Dimensional Materials and Application Technology of Ministry of Education, Xiangtan University, Xiangtan 411105, China;
 - 3. China Railway Eryuan Engineering Group Co., Ltd., Chengdu 610000, China

Received 20 June 2020; accepted 18 January 2021

Abstract: The microstructure and properties of the as-cast, as-homogenized and as-extruded Mg-6Zn-4Sn-1Mn (ZTM641) alloy with various Al contents (0, 0.5, 1, 2, 3 and 4 wt.%) were investigated by OM, XRD, DSC, SEM, TEM and uniaxial tensile tests. The results show that when the Al content is not higher than 0.5%, the alloys are mainly composed of α -Mg, Mg₂Sn, Al₈Mn₅ and Mg₇Zn₃ phases. When the Al content is higher than 0.5%, the alloys mainly consist of α -Mg, Mg₂Sn, MgZn, Mg₃₂(Al,Zn)₄₉, Al₂Mg₅Zn₂, Al₁₁Mn₄ and Al₈Mn₅ phases. A small amount of Al (\leq 1%) can increase the proportion of fine dynamic recrystallized (DRXed) grains during hot-extrusion process. The room-temperature tensile test results show that the ZTM641-1Al alloy has the best comprehensive mechanical properties, in which the ultimate tensile strength is 332 MPa, yield strength is 221 MPa and the elongation is 15%. Elevated-temperature tensile test results at 150 and 200 °C show that ZTM641-2Al alloy has the best comprehensive mechanical properties.

Key words: Mg-Zn-Sn-Mn alloy; Al; microstructure; mechanical properties; dynamic recrystallization; nucleation

1 Introduction

Mg alloys are widely used in many fields such as transportation, electronics and military industries, due to their low density, high specific strength, specific stiffness and excellent damping properties [1–3]. However, the widespread application of Mg alloys is still limited due to their low absolute strength and poor formability [4–6]. Thus, it is essential to develop some high-strength and low-cost wrought Mg alloys to expand their application area.

Among various Mg alloy systems, a new heat-treatable wrought Mg-Zn-Sn alloy has attracted more and more attention due to the

thermal Mg₂Sn phase and typical precipitation strengthening Mg-Zn phases [7,8]. However, the Mg₂Sn phase is coarse and the hardening behavior of Mg-Zn phases is unsatisfactory, which leads to unfavorable mechanical properties of Mg-Zn-Sn [9,10]. further improving Thus, mechanical properties of Mg-Zn-Sn alloy has become the current research direction. It is well known that alloying is an effective method to improve the mechanical properties of Mg alloys, mainly due to the formation of new secondary phases or refinement of phases [11-13]. In the recent years, alloying elements of Mg-Zn-Sn are mainly Y [14], Sb [15], Mn [16-18], Ca [19], Al [20] and other elements. Although the rare earth elements can effectively improve the mechanical

properties and creep resistance of Mg alloys, the relatively high cost also limits the application of rare earth Mg alloys [21]. Thus, non-rare earth elements have attracted more and more attention. Among them, Al and Mn are promising alloying elements to improve mechanical properties of Mg alloys. As for Al element, on one hand, it is reported that excessive Al will precipitate Mg₁₇Al₁₂ phase at a low eutectic temperature instead of thermal Mg₃₂(Al,Zn)₄₉ phase [22]. Obviously, the content of Al plays an important role in the mechanical properties of Mg-Zn alloys and is worthy to be explored. On the other hand, it is reported that Al can effectively improve the mechanical properties due to decreasing grain size and Al solute atoms [23]. As for Mn element, researchers have found that adding a small amount of Mn (≤ 0.6 wt.%, here after all compositions are in mass fraction unless stated otherwise) to Mg alloys can reduce the content of Fe impurities and thus reduce the corrosion rate [24,25]. Nevertheless, the function of Mn is more than that. Recently, YU et al [26] have found that Al would preferentially combine with Mn to form Al-Mn phases with a high eutectic temperature. The results show that Al-Mn phases may play an important role in elevated temperature performance. At present, there are few studies on the effect of the combined addition of Al and Mn on the microstructure and properties of Mg-Zn-Sn alloy.

QI et al [27] researched the effect of Sn addition on the microstructure and mechanical properties of Mg-6Zn-1Mn alloy, and found that the as-extruded Mg-6Zn-4Sn-1Mn (ZTM641) alloy had the highest ultimate tensile strength (331 MPa) and yield strength (272 MPa), but the elongation was slightly low, 10.76%. In order to comprehensive obtain the best mechanical properties of the alloy, we try to add Al element to ZTM641 alloy to explore a novel high-performance Mg alloy, and to investigate the effect of Al addition on the microstructure and mechanical properties of ZTM641 alloy in the present work. It is hoped that the research can provide the necessarily theoretical and experimental basis to prepare Mg alloys with better mechanical properties.

2 Experimental

The alloy ingots with nominal compositions of

ZTM641-xA1 (x=0, 0.5, 1, 2, 3 and 4 wt.%) were prepared by commercially pure Mg (≥99.9 %), pure $Zn (\ge 99.9 \%)$, pure $Sn (\ge 99.9 \%)$, pure $Al (\ge 99.9 \%)$ and Mg-4.10%Mn master alloys. Since the melting point of Mn element is 1244 °C, which is too higher compared with the melting point of 648 °C of Mg element, it cannot be smelted by traditional methods. According to the Mg-Mn phase diagram, the melting point of the Mg-Mn master alloy is basically close to the Mg melting point, which reduces the temperature required for subsequent alloy smelting. All materials were melted in an electrical resistance furnace under CO₂ with a spot of SF₆ protective gas to prevent oxidation, and then cast into a steel mold. The ingots were then homogenized at 330 °C for 24 h followed by air cooling. The homogenized ingots were extruded into rods at 350 °C with an extrusion ratio of 25, and the extrusion speed was 2 m/min.

The mechanical properties of the as-extruded samples were evaluated by tensile tests at room temperature (RT), 150 and 200 °C. Tensile tests were carried out at a strain rate of 2 mm/min using an INSTRON 3369 electronic universal material testing machine. Mechanical properties were determined by a complete stress-strain curve. The ultimate tensile strength (UTS), yield strength (YS) and the elongation to failure (EL) were obtained based on the average of five tests.

The optical microstructure (OM) was observed by an Olympus BX53M. Phase constitutions were determined by an U1tima IV X-ray diffractometer using a Cu K_{α} radiation with a scanning angle from 10° to 90° and a scanning rate of 4 (°)/min. The scanning electron microscopy (SEM) observation was examined by a JSM-6360 scanning electron microscope equipped with an Oxford INCA Energy 350 energy dispersive spectrometer. Thermal analysis was carried out by using the NETZSCH STA 449C differential scanning calorimeter, and the heating curves were recorded at 50–750 °C. The transmission electron microscopy (TEM) observation was FEI Tecnai G2 F20 equipped with energy-dispersive spectroscopy (EDS) detectors.

3 Results and discussion

3.1 Microstructure evolution

3.1.1 As-cast microstructure

The XRD patterns of the as-cast ZTM641-xAl

alloys are shown in Fig. 1. It can be seen that ZTM641 alloy mainly contains α-Mg, α-Mn, Mg₂Sn and Mg₇Zn₃ phases. When the Al content is 0.5%, the α-Mn phase disappears and the Al₈Mn₅ phase is formed. When the Al content are 1% and 2%, the test alloys are composed of α-Mg, Mg₃₂(Al,Zn)₄₉, Al₂Mg₅Zn₂, MgZn, Al₈Mn₅, Al₁₁Mn₄ and Mg₂Sn phases. When the Al content increases to 3% and 4%, the test alloys consist of α-Mg, Mg₃₂(Al,Zn)₄₉, Al₂Mg₅Zn₂, Al₈Mn₅, Al₁₁Mn₄ and Mg₂Sn phases. In order to accurately verify the phases, further experiments on the as-cast alloys were carried out with SEM.

The backscatter electron (BSE)-SEM images of the as-cast ZTM641–xAl alloys are shown in Fig. 2. It can be seen from Fig. 2 that all the cast alloy structures consist of α -Mg dendrites and

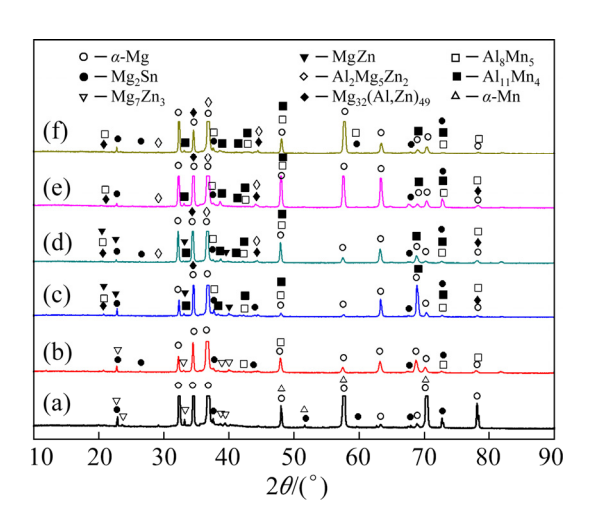


Fig. 1 XRD patterns of as-cast ZTM641-xA1 alloys: (a) x=0; (b) x=0.5; (c) x=1; (d) x=2; (e) x=3; (f) x=4

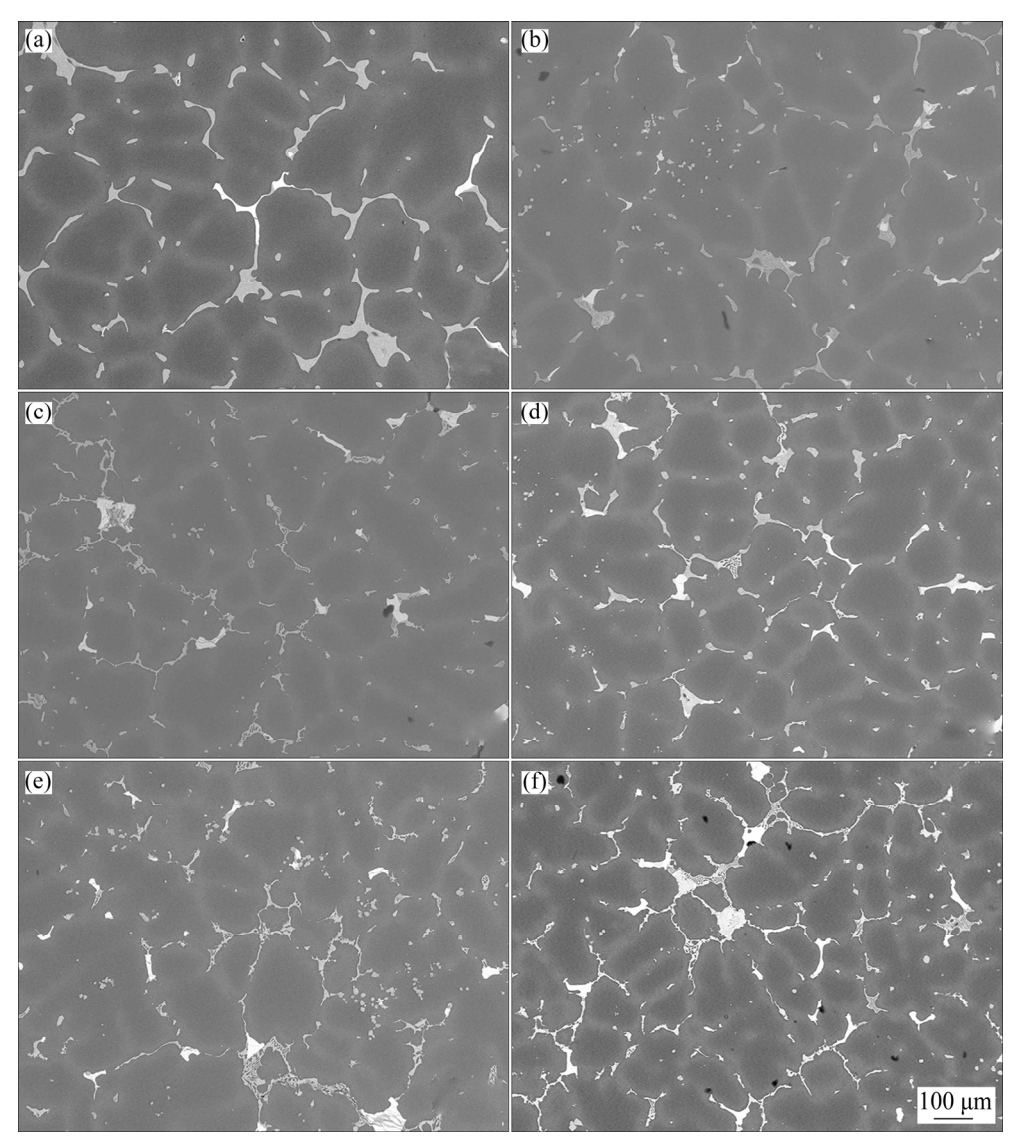


Fig. 2 Low magnification BSE-SEM micrographs of as-cast ZTM641-xAl alloys: (a) x=0; (b) x=0.5; (c) x=1; (d) x=2; (e) x=3; (f) x=4

eutectic compounds between dendrites. As the Al content increases, the volume fraction of the eutectic compounds gradually increases, and the dendrites are refined to some extent. This is because the enrichment of solute elements at the solid–liquid interface hinders crystal grain growth, and forms subcooled components, which can provide driving force for nucleation in the subcooled zone, thus playing a role in grain refinement. The growth restriction factor (GRF) is usually used to characterize the segregation ability of solute elements [28]:

$$GRF=mC_0(k-1) \tag{1}$$

where m is the liquidus slope, C_0 is the concentration of the solute in binary alloy, and k is the partition coefficient. The GRF value reflects the ability to form a stable crystal nucleus in melt. The larger the GRF factor value, the more obvious the grain refinement effect of the solute element. According to Eq. (1) and the corresponding Refs. [29,30], the GRF values of Zn, Sn, Al and Mn element are 5.31, 1.47, 4.32 and 0.15, respectively, which indicates that Al element has a good potential to refine the structure of the cast alloys.

To further confirm the types of phases, the typical phases in Fig. 3 were analyzed by EDS, and the results are summarized in Table 1. The EDS results show that the bright white phase in Fig. 3 is mainly composed of Mg and Sn, with a mole ratio of about 2:1, which can be determined as the Mg₂Sn phase by combining XRD results. As shown

in Figs. 3(a) and (b), when the Al content is not higher than 0.5%, the dark color phase mainly contains Mg and Zn elements, and the Mg/Zn mole ratio is about 7:3, which can be identified as Mg₇Zn₃ phase by combining XRD results. However, when Al is higher than 1%, Mg₇Zn₃ phase becomes MgZn phase. The Mg₇Zn₃ phase is metastable and will be gradually replaced by the MgZn equilibrium phase [31]. It is suggested that Al element may promote the metastable phase transition process. In addition, the EDS results in Table 1 cannot distinguish MgZn, Mg₃₂(Al,Zn)₄₉ and Al₂Mg₅Zn₂ phases well. This may be mainly because the atomic radii of Zn and Al are closer (Mg 15.99 nm, Al 14.32 nm, Zn 13.33 nm), and Al and Zn may replace each other [32]. Although the components of the phases discussed above are analogous, the type of phases can be presumed on the basis of mole ratio and morphology. From the results of F and I points, it can be seen that with the increase of Al content, the morphology of Al₂Mg₅Zn₂ changes from blocky to network. When Al is less than 2% and the mole ratio of Mg/Zn is about 1:1, MgZn exists as a continuous elongated strip. Although Al element is detected, it is the result of elemental segregation and atomic substitution just discussed above. Mg₃₂(Al,Zn)₄₉ phase exists as bone-like phase in the alloys, and mole ratio of Al to Zn in Mg₃₂(Al,Zn)₄₉ phase is about 50:1. Thus, I and G points can be presumed to be Al₂Mg₅Zn₂ and Mg₃₂(Al,Zn)₄₉ phases, and the results are consistent with previous report [33]. Furthermore, it can be

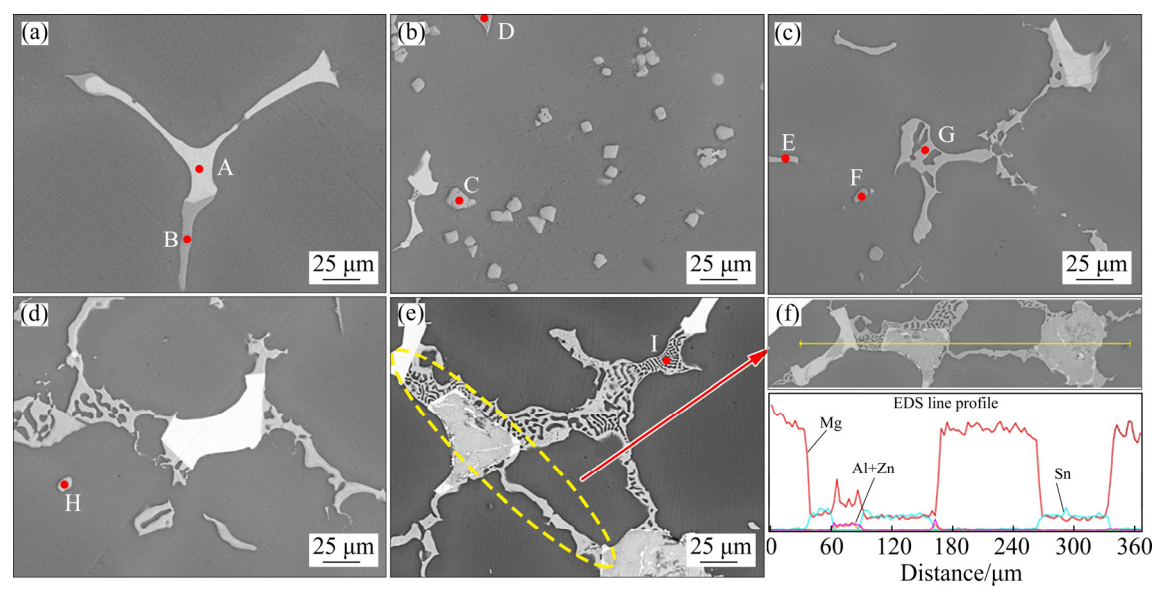


Fig. 3 High magnification BSE-SEM micrographs of as-cast ZTM641-xAl alloys: (a) x=0; (b) x=0.5; (c) x=1; (d) x=2; (e) x=4; (f) EDS line profile in (e)

Table 1 EDS results of as-cast ZTM641-xAl alloy

Position	Composition/at.%					Dlassa
	Mg	Zn	Sn	Mn	Al	Phase
A	63.54	_	34.57	-	_	Mg_2Sn
В	66.83	33.17	_	_	_	Mg_7Zn_3
C	_	_	_	62.78	31.22	Al_8Mn_5
D	68.30	29.95	_	_	1.34	Mg_7Zn_3
E	45.53	40.14	_	_	14.41	MgZn
F	66.54	21.47	_	_	11.76	$Al_2Mg_5Zn_2$
G	46.01	35.67	_	_	18.29	Mg ₃₂ (Al,Zn) ₄₉
Н	3.52	_	_	45.18	50.93	$Al_{11}Mn_{4} \\$
I	63.60	19.27	-	-	16.94	$Al_2Mg_5Zn_2$

seen from C and H points that the Al_8Mn_5 and $Al_{11}Mn_4$ phases are the main Al–Mn phases exiting in the studied alloys. This indicates that Al tends to combine with Mn, and there is no significant difference in morphology of different types of Al–Mn phases, which is consistent with the previous study [34].

Apparently, the mass ratio of Zn/Al plays a crucial role in the phase formation. With the increase of Al content, the transformation sequence of the phase related to Zn or Al is as follows: $Mg_7Zn_3 \rightarrow Mg_{32}(Al,Zn)_{49} + MgZn \rightarrow Mg_{32}(Al,Zn)_{49} +$ Al₂Mg₅Zn₂. When the Zn/Al mass ratio is less than 6:1, the corresponding Al-containing phases are mainly composed of Al-Mn phase. When the Zn/Al mass ratio is greater than 3:1 and less than 6:1, the corresponding Al- or Zn-containing phases are mainly composed of Mg₃₂(Al,Zn)₄₉ and MgZn phases. When the Zn/Al mass ratio is greater than 1.5:1 and less than 3:1, the corresponding Al- or Zn-containing phases are mainly composed of Mg₃₂(Al,Zn)₄₉ and Al₂Mg₅Zn₂ phases. In order to verify this result, the DSC was further conducted to study the phase transition.

The DSC curves of the as-cast ZTM641-xAl alloys are shown in Fig. 4, and the detailed information is shown in Table 2. For all experimental alloys, Peak 1 during the heating is the melting temperature of the alloys. With the increase of Al content, the melting temperature gradually decreases from 622.92 to 593.27 °C, which indicates that the Al addition is beneficial to reducing the casting temperature and improving the casting performance of the alloys. According to the

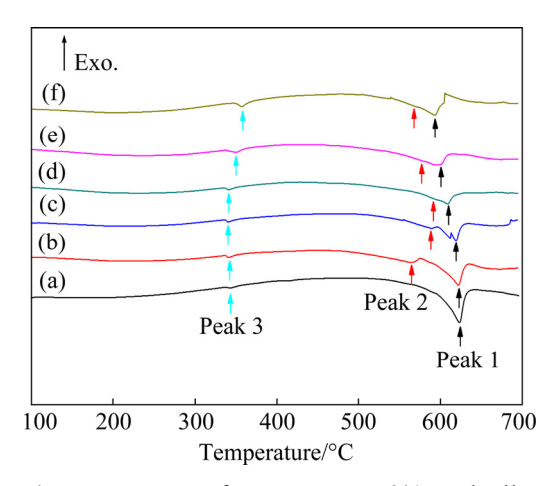


Fig. 4 DSC curves of as-cast ZTM641-xAl alloys at heating rate of 10 K/min: (a) x=0; (b) x=0.5; (c) x=1; (d) x=2; (e) x=3; (f) x=4

Table 2 Data of DSC peaks for as-cast ZTM641-xAl in Fig. 4

A 11	Heating temperature/°C					
Alloy	Peak 1	Peak 2	Peak 3			
ZTM641	622.92	-	342.44			
ZTM641-0.5Al	622.92	565.43	342.41			
ZTM641-1Al	619.44	588.89	339.74			
ZTM641-2A1	610.67	590.69	340.64			
ZTM641-3A1	597.65	576.77	349.40			
ZTM641-4Al	593.27	566.33	357.14			

above microstructural analysis, the compounds in ZTM641 alloy are mainly composed of Mg₂Sn and Mg₇Zn₃ phases. Combined with the Mg-Zn-Sn ternary phase diagram, it can be inferred that the following eutectic reaction occurs at the Peak 3 (342.44 °C): $L \rightarrow \alpha$ -Mg + Mg₂Sn + Mg₇Zn₃ [35]. As the Al content increases to 0.5%, Peak 2 appears at 565.43 °C, corresponding to the α -Mg and Al₈Mn₅ phases [36]. If the quantity of Al-Mn phases is relatively limited, the heat transformation will be small during phase transition process and the precipitation temperature of Al-Mn phase is higher than that of α -Mg [37,38]. Thus, it is difficult accurately detect the melting temperature of Al-Mn phase in the DSC curve. However, the solid solubility of Mn in the α -Mg, Mg₂Sn and Mg-Zn-Al phases is slight, so it can be inferred that all Mn elements are formed as Al-Mn phases in the ZTM641-xAl alloys. According to the above microstructure and previous report [39–41],

as the Al content increases to 1%, it can also be inferred that the following reaction occurs at Peak 3 (339.74 °C): $L \rightarrow \alpha$ -Mg + Mg₃₂(Al,Zn)₄₉ + MgZn + Mg₂Sn. Finally, combined with the above discussion, for ZTM641–3Al and ZTM641–4Al alloys, the following eutectic reaction occurs at the Peak 3: $L \rightarrow \alpha$ -Mg + Al₂Mg₅Zn₂ + Mg₃₂(Al,Zn)₄₉ + Mg₂Sn.

3.1.2 As-homogenized microstructure

The homogenization treatment before hot extrusion not only can dissolve the eutectic compound, eliminate dendrite segregation, and improve the non-uniformity of the as-cast structure composition, but also can greatly reduce the plastic deformation resistance of the alloy and improve the

forming performance. Figure 5 shows the BEM-SEM images of the as-homogenized ZTM641–xAl alloys. It can be seen that most of the non-equilibrium segregated phases between the dendrites are dissolved in the matrix. When the Al content is low, most of the eutectic compounds are dissolved, and the homogenization effect is better. When the Al content is high, that is, in the case of a low Zn/Al mass ratio, the volume fraction of the bright Mg₂Sn bulk phase, Al–Mn particle phase, strip-like MgZn phase and Mg–Zn–Al phase increases, and the homogenization effect becomes worse. It can be attributed to the good thermal stability of these phases and limited solubility of the matrix.

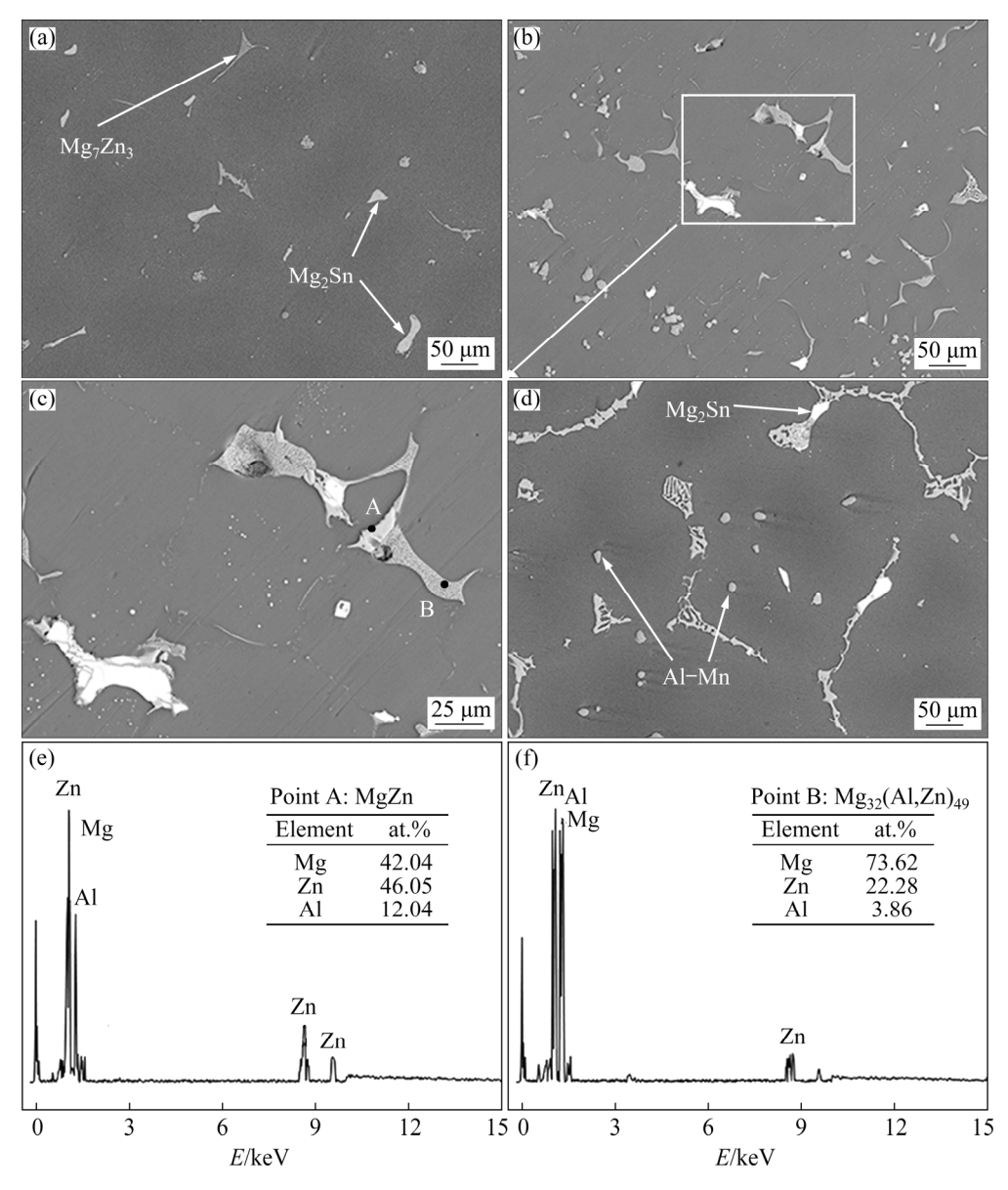


Fig. 5 BSE-SEM micrographs of as-homogenized ZTM641-xAl alloys: (a) x=0; (b) x=2; (c) Enlargement of circular rectangular part in (b); (d) x=4; (e, f) Corresponding EDS results of points in (c)

3.1.3 As-extruded microstructure

Figure 6 shows the optical microstructures of the as-extruded ZTM641–*x*Al alloys, taken from the parallel plane to the extrusion direction (ED). Due to the DRX during the hot extrusion process, the grain structure of all alloys is significantly refined. In order to better show the grain size of the alloy, the grain size of the as-extruded sample is calculated by using Heyn transversal method. The calculation formula of the average grain size is as follows:

$$d = \frac{L}{N_L} = \frac{L}{NM} \tag{2}$$

where d is the average grain size, N_L is the number of cut grains per unit line length, L is the length of the secant line, N is the total number of cut grains, and M is the magnification of the photo. Line is introduced to pass through the grain, and the

number of grains passing through the line is counted. The average value is calculated after several measurements, and the size of the grain is counted. Among them, the ZTM641 alloy has a mixed crystal structure, shown in the orange and white ovals, and the grain size of ZMT614 alloy is calculated to be 5.9 µm. The second phase remaining after homogenization treatment is broken into small particle phases during the extrusion process, and these dispersed particles play an important role in hindering recrystallization. After adding 1% Al, the structure is refined, and the grain size is reduced to 4.9 µm. However, when the Al content exceeds 1%, the bulk second phase gradually increases, and the grain size increases. As shown in Figs. 6(d) and (f), with the further Al content, the grain size gradually increases, after calculation, it increases from 5.2 to 5.6 μm.

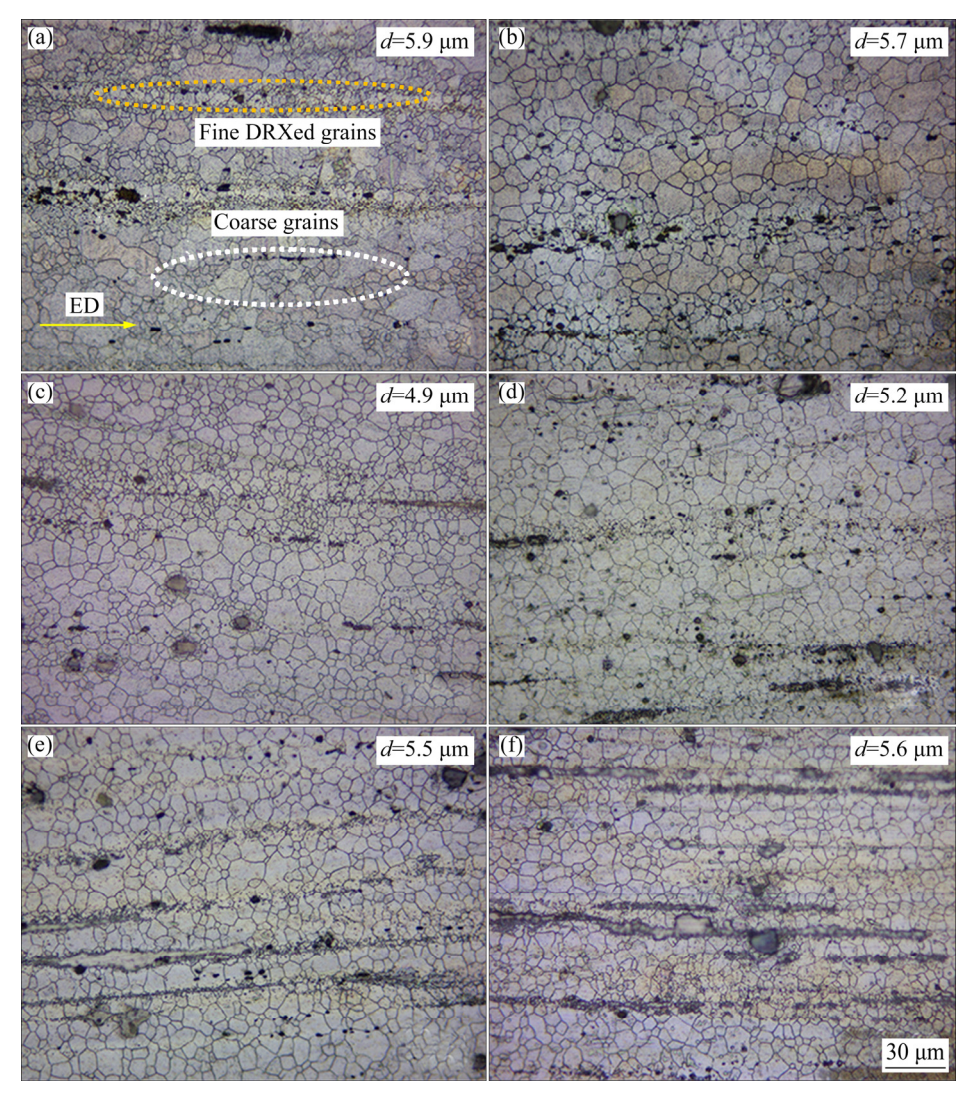


Fig. 6 Optical micrographs of as-extruded ZTM641-xAl alloys: (a) x=0; (b) x=0.5; (c) x=1; (d) x=2; (e) x=3; (f) x=4 (Extruded direction is horizontal)

STJOHN et al [42] proposed the interdependence theory, believing that the grain size $(d_{\rm gs})$ is the result of the interdependence of nucleation and growth, and then deduced the prediction formula of grain size, which is expressed as follows:

$$d_{\rm gs} = x_{\rm cs} + x_{\rm dl} + x_{\rm sd} \tag{3}$$

where x_{cs} is the distance that the previous grain must grow to generate sufficient component supercooling; $x_{\rm dl}$ is the diffusion length from the solidliquid interface at x_{cs} of the previously nucleated grain, where component supercooling reaches its maximum value. The sum of x_{cs} and x_{dl} , denoted by $x_{\rm nfz}$, represents the length of the nucleation-free zone, and $x_{\rm sd}$ is the distance between $x_{\rm nfs}$ and the next most potent particle in the melt. This model explains, to a certain extent, why the grain size does not continue to be refined when there are enough nucleating particles after the increase of Al content. This is due to the fact that only a part of the second phase particles can play the role of heterogeneous nucleation. When the previous nucleation particles cannot provide enough supercooling for the next particle, the remaining heterogeneous nucleation particles cannot produce nucleation, and the heterogeneous nucleation process cannot continue.

It is well known that during hot deformation, second phases of different sizes can promote or inhibit DRX behavior. The small second phase (less than 1 µm) hinders DRX because it prevents the formation of the lattice curvature required for nucleation and then pins grain boundaries. When the size of the second phase is larger (greater than 1 μm), it will increase the dislocation density around them, thereby promoting DRX [43]. However, due to the roughness of the second phase, the range involved in the pinning becomes weak, resulting in grain size growth. For the experimental alloys, as the Al content increases, the type and size of the second phases are different, which play a different role in the DRX process during plastic deformation. Therefore, when Al is greater than 2%, the fine second phase gradually decreases and the coarse second phase increases, that is, the extrusion streamline gradually becomes larger, and the grain size increases instead, which is consistent with the result in Fig. 6.

To determine the morphology and composition of the extrusion streamlines, the ZTM641–xAl alloys samples are analyzed by XRD and SEM, as

shown in Figs. 7 and 8. It can be seen from Fig. 8 that the residual second phases after the homogenization process are broken into small particles during the extrusion process and rearranged along the ED. The Al₈Mn₅ particles appear as the Al content increases to 0.5%. After that, Al₈Mn₅ phases are transformed into Al₁₁Mn₄ phases, which can be confirmed in Fig. 7. And the quantity of streamlines further increases obviously (2% Al). It is expected that due to the resolution limitation of SEM, the fine and dispersive phases cannot be observed. Thereby, in order to accurately identify the precipitates, TEM study is further conducted on the as-extruded ZTM641–1Al alloy.

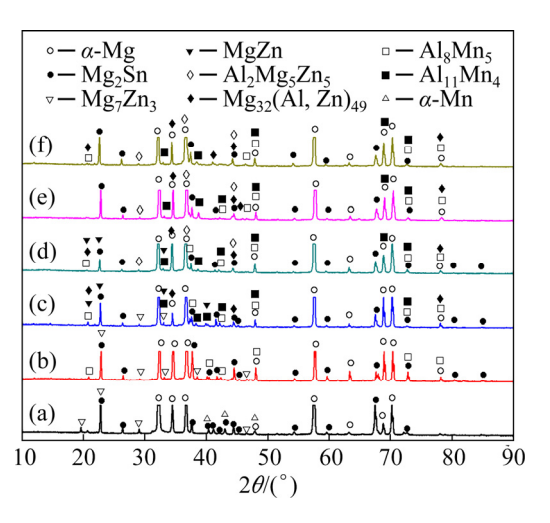


Fig. 7 XRD patterns of as-extruded ZTM641–xAl alloys: (a) x=0; (b) x=0.5; (c) x=1; (d) x=2; (e) x=3; (f) x=4

Figures 9(a-c) show the bright field (BF) images and selected area electron diffraction (SAED) patterns obtained from the eutectic phases of the as-extruded ZTM641-1Al alloy, based on the incident beam parallel to the [0001] and $[\overline{1}2\overline{1}1]$ of the α -Mg. It is found that there is a large rod-shaped phase on the base surface of the Mg matrix, which plays an important role in preventing dislocation slippage. As marked by yellow arrows, during the extrusion process, dislocations accumulate around the second phase. According to the EDS results in Figs. 9(e, f), a small quantity of Al is checked. It can be speculated that Al atoms may dissolve in MgZn phase, deform its lattice, and increase the lattice parameter, which is consistent well with the previous report [31]. Figure 9(d) shows the HRTEM of a rod-like phase with a width of 15 nm, and combined with the analysis in Section 3.1.3, it can be presumed as a small MgZn phase.

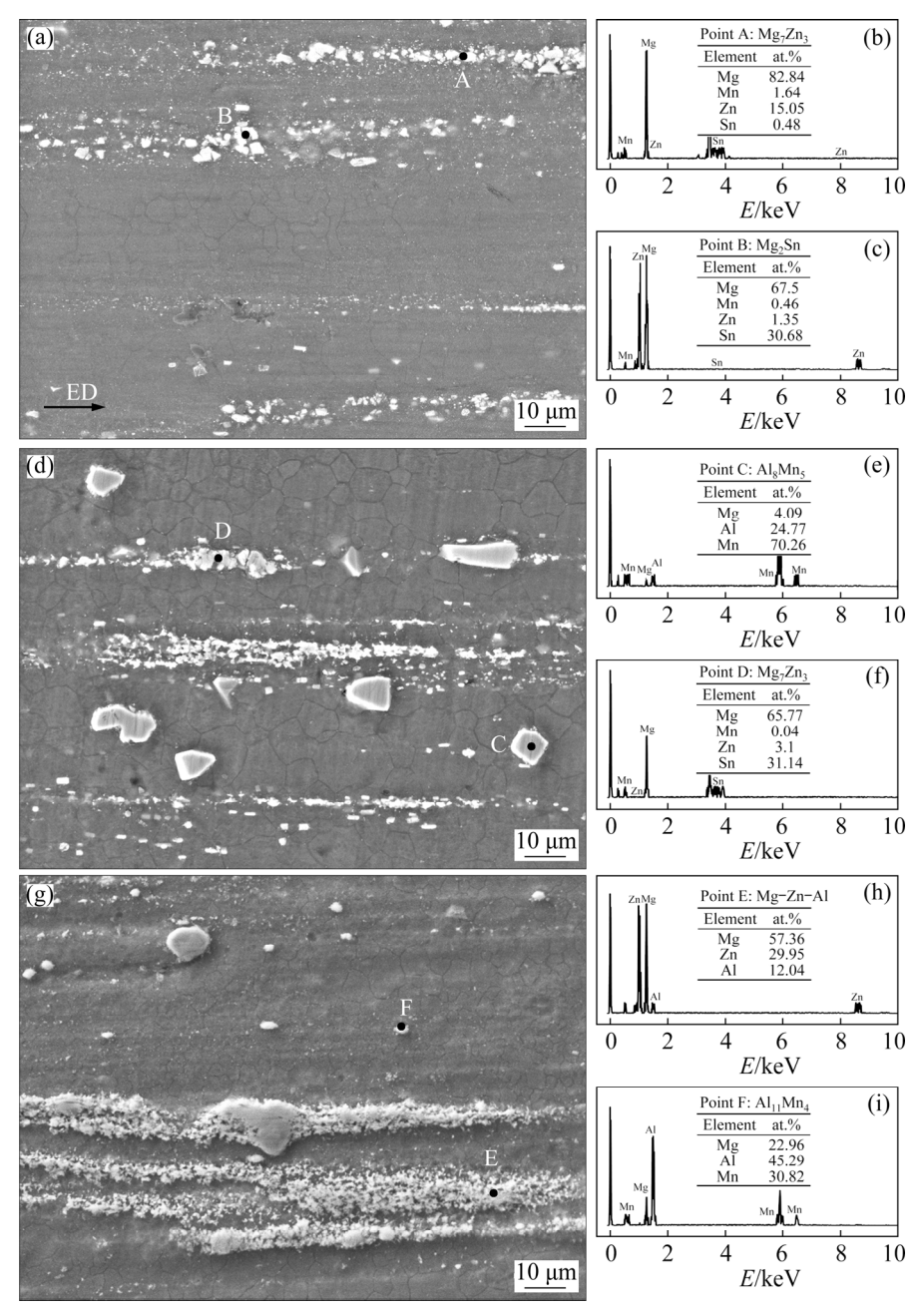


Fig. 8 BSE-SEM micrographs (a, d, g) and EDS results (b, c, e, f, h, i) of as-extruded ZTM641-xAl alloys: (a, b, c) x=0; (d, e, f) x=0.5; (g, h, i) x=2

In addition, as marked with blue and purple frames (Fig. 9(c)), many nanoscale rod-like and disc-like phases are formed within the Mg matrix. For the purple frame, the number density of rod-like MgZn phases marked as purple arrow are evidently higher than that of disc-like phases, but the opposite result is obtained in the blue frame. Some disc-like phases are Mg₂Sn phase, whose orientation relationship (OR) with the Mg matrix is uncertain [27,44]. The others are Mg₃₂(Al,Zn)₄₉ phase, which has a complicated OR with the Mg matrix [45]. In addition, MgZn phase

in Fig. 9(c) plays a vital role in pinning the dislocation.

The BF-SEM images of nano-polycrystalline and HAADF- STEM images of Al₈Mn₅ are shown in Fig. 10. A number of long ribbon-like bright nano-polycrystallines are observed in Figs. 10(a) and (b), combined with the EDS of Point C, which are mainly composed of Mg, Zn and a bit of Sn elements. It can be determined that the Point C is Mg matrix. Further observation of Fig. 10(b) reveals that the second phases with small particle size are scattered in the ribbon-like bright nano-

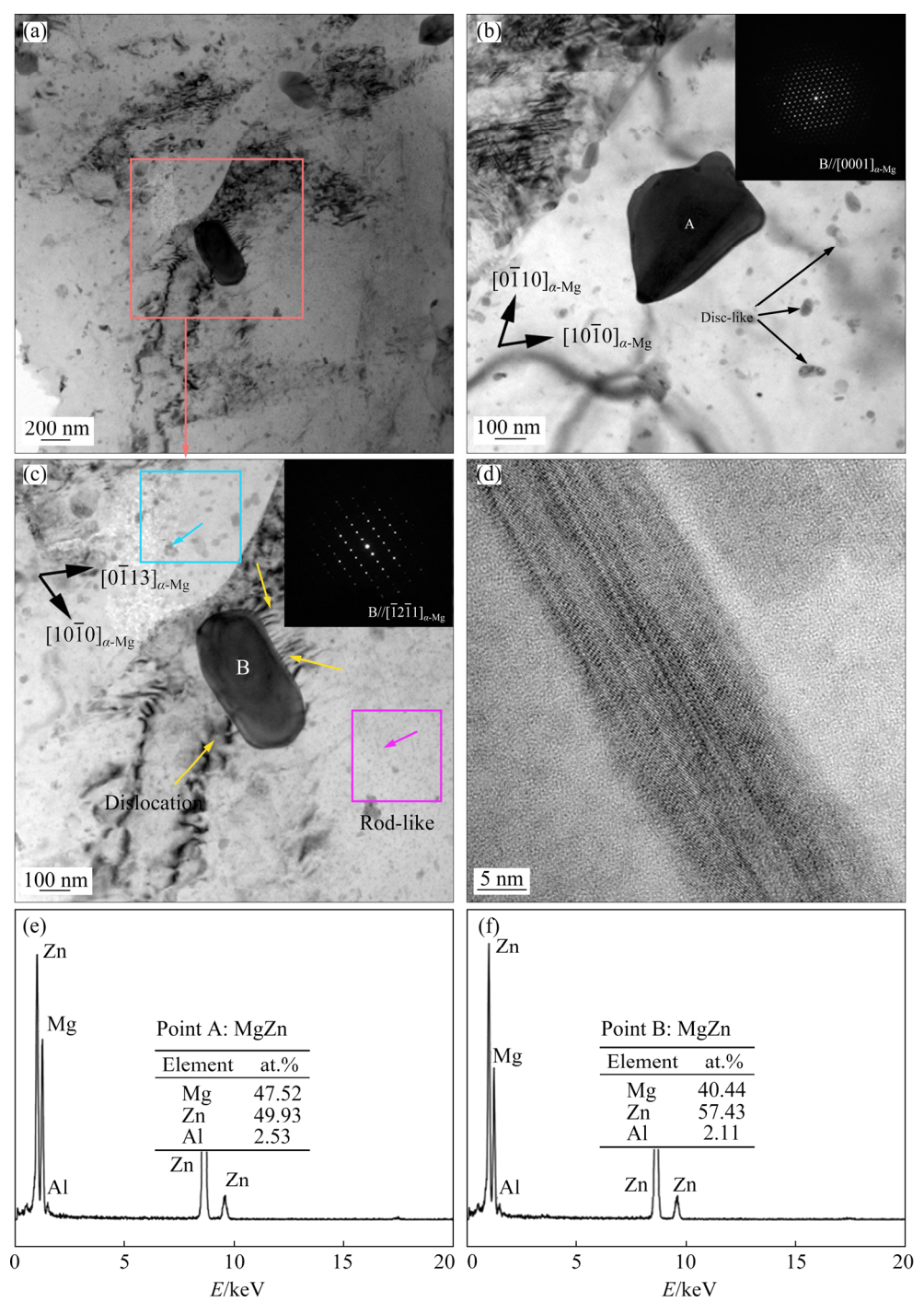


Fig. 9 TEM micrographs (a, b, c, d) and EDS results (e, f) of as-extruded ZTM641-1Al alloy: (a) BF-TEM image; (b) BF-TEM image, taken along $[0001]_{\alpha-Mg}$ zone axis; (c) BF-TEM image, taken along $[\overline{1}2\overline{1}1]_{\alpha-Mg}$ zone axis; (d) HRTEM image of rod-like phase; (e, f) EDS results of Points A and B in (b) and (c), respectively

polycrystalline. At the same time, the dislocation stacking is found around the nano-polycrystalline, and a large number of dislocations terminate at the edge of the polycrystalline. Nano-polycrystalline is an important factor affecting DRX and mechanical properties of the experimental alloys, but the formation and strengthening mechanisms are unclear. In order to analyze this nano-

polycrystalline clearly, further experiments are needed. The Al_8Mn_5 phase precipitates dynamically during the extrusion process, as shown in Fig. 10(c). It is reported that there is no clear OR between Al_8Mn_5 and α -Mg [46]. The average size of the Al_8Mn_5 particle is about 3–6 μ m in Fig. 10(c) and Fig. 8, which is consistent with the report in Ref. [26].

3.2 Mechanical properties

3.2.1 Mechanical properties at RT

Figure 11(a) shows the density of the as-extruded ZTM641-xAl alloy. It can be seen that

as the Al content increases, the density increases from 1.79 to 1.86 g/cm³. Comparing with the Ref. [47], it is found that the density of the experimental alloys is basically the same as that of

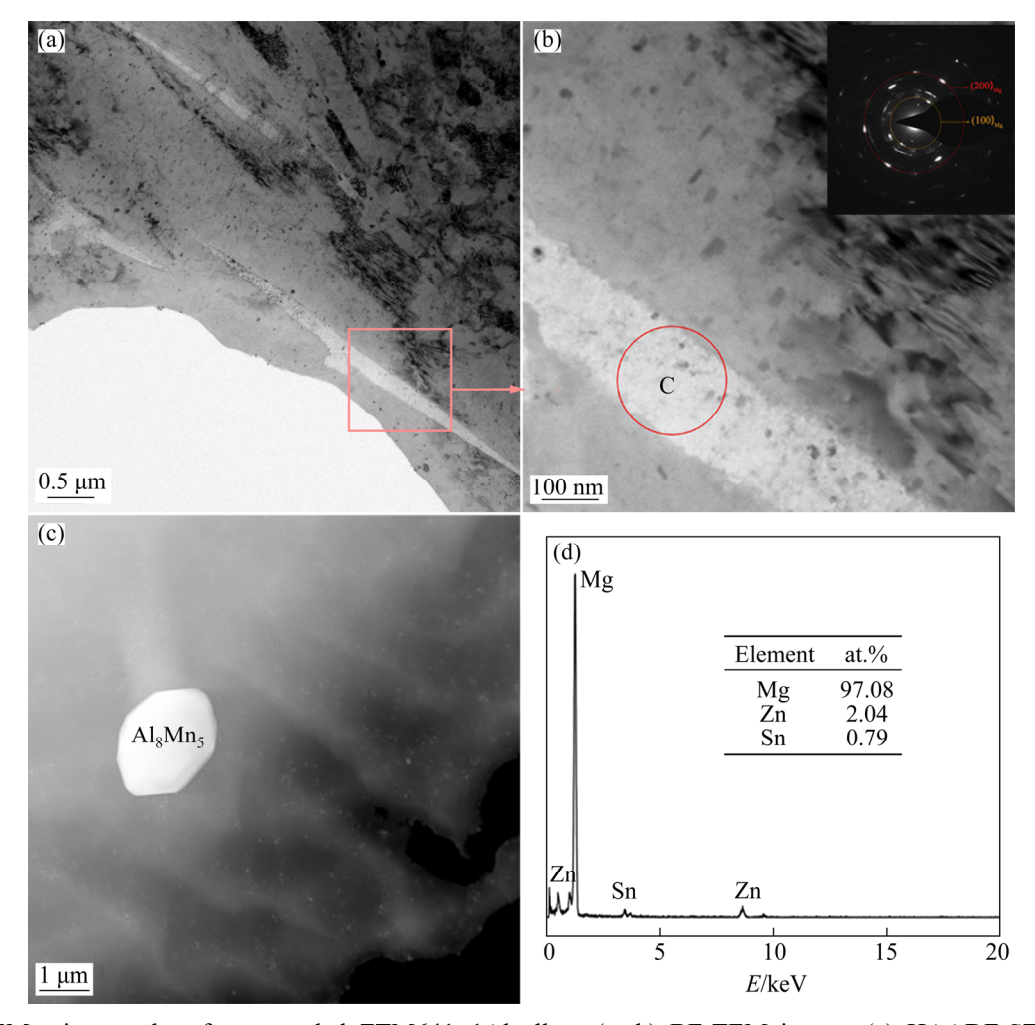


Fig. 10 TEM micrographs of as-extruded ZTM641-1Al alloy: (a, b) BF-TEM image; (c) HAADF-STEM image; (d) EDS results of Point C in (b)

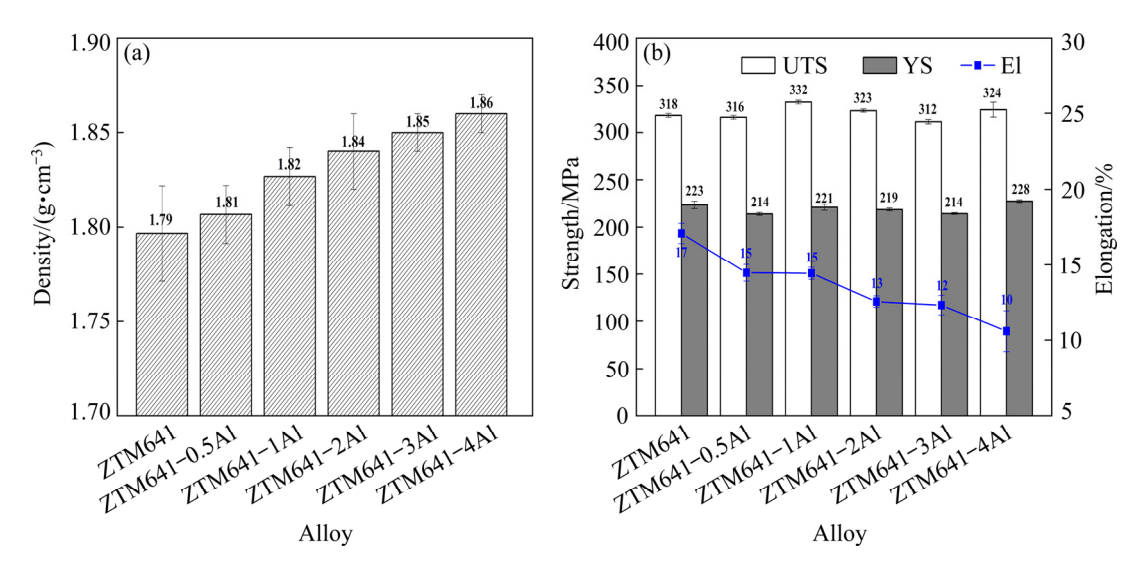


Fig. 11 Densities (a) and mechanical properties (b) of as-extruded ZTM641-xAl alloys at RT

the commercial high-strength ZK60 alloy. Figure 11(b) shows the mechanical properties of the as-extruded ZTM641-xAl alloys at RT. The results show that as the Al content increases, the strengths of the alloys are similar, among which the 1% Al alloy is higher, reaching 332 MPa, while the elongation of the alloy is gradually reduced. As mentioned earlier, after adding a small amount of Al, the grains of the alloys are refined to a certain extent, which is beneficial to improving the mechanical properties. As the Al content further increases, the bulk second phase increases, which becomes a source of cracks, resulting in a decrease in elongation.

Figures 12(a-d) show the secondary electron (SE) and BSE-SEM images of the tensile fractures of the as-extruded ZTM641 and ZTM641-2Al

alloys at RT. From SE-SEM images, it can be seen that the fracture is mainly composed of cleavage plane, dimples, tear edges and granular bumps, indicating that the fracture mode of the alloy is mixed fracture. BSE-SEM can be used to observe the distribution of the second phase on the fracture surface of the experimental alloys. For the ZTM641 alloy, combined with the above microstructure analysis, the second phases are white or gray phases, that is, the phases of the fracture surface are MgZn and Mg₂Sn mixed compounds. For the ZTM641-2Al alloy, it can be seen that the size and number of the second phase are slightly larger than those of the ZTM641 alloy, and some of the second phases are fractured with cracks in the middle. It is presumed that the crack may originate from the bulk second phase. It is well known that the stress

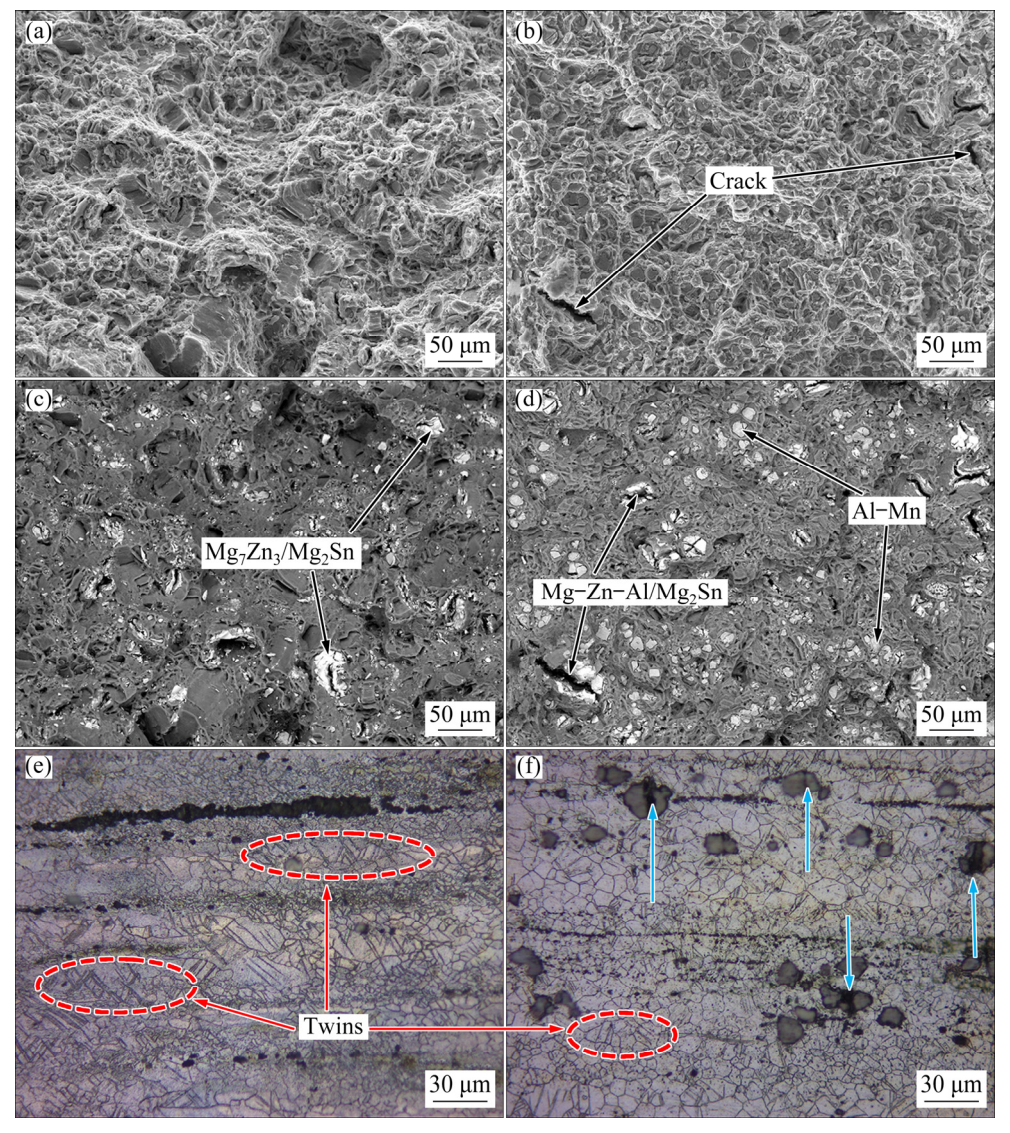


Fig. 12 SE-SEM (a, b) and BSE-SEM (c, d) micrographs of fracture surface, and optical images from longitudinal sections adjacent to fracture surface (e, f) of as-extruded ZTM641-xAl alloy at RT: (a, c, e) x=0; (b, d, f) x=2

concentration occurs due to different deformation capabilities of the matrix and the second phase, and the stress concentration easily occurs on the relatively large second phase, which easily leads to the formation of microcracks. Therefore, when the Al content is low, the grains of alloy are refined and the strengths are improved, but with the further increase of the Al content, the bulk second phase increases, which becomes the crack source and the elongation gradually decreases.

In order to better observe the origin and propagation of cracks, the longitudinal sections of fracture surface of the as-extruded ZTM641 and ZTM641-2A1 allovs are metallographically observed, as shown in Figs. 12(e) and (f). It can be seen that the twins mainly appear within the coarse grains. In addition, most cracks originate from the second phases that generate concentration, and the cracks preferentially expand in the middle of the large second phase, that is, the second phases fracture. In a word, the fracture mode of the experimental alloys is transgranular fracture.

3.2.2 Mechanical properties at elevated temperatures

Figure 13 shows the mechanical properties of the as-extruded alloys at elevated temperatures (150 and 200 °C). It can be seen that when the tensile temperature is 150 °C, as the Al content increases, the elongation gradually increases from 59% to 71%. And the strength of the alloys increases first and then decreases. Among them, ZTM641-2Al alloy has the best strength, that is, UTS and YS are 171 and 140 MPa, respectively. The reason for this phenomenon is that after Al element is added to ZTM641 alloy, Al and Mn elements combine to form Al-Mn phase, which is a thermostable high-temperature phase and can significantly improve the high temperature strength of the alloy. However, when the Al content is too high, the size of generated Al-Mn phase is too large, which is not conducive to the coordinated deformation of the alloy, resulting in the decrease of the alloy strength. When the tensile test is performed at 200 °C, the mechanical properties show the same changes. Among them, ZTM641-2Al alloy has the best mechanical properties, that is, UTS, YS and EL are 105 MPa, 93 MPa and 74%, respectively. It is generally known that the deformation modes of Mg alloys at elevated temperatures are mainly the movement of dislocations and the slippage of grain boundaries. Therefore, after the Al addition, the high-melting second phases, such as Al₈Mn₅ and Mg₂Sn, will be formed for the experimental alloys. During the extrusion process, not only the bulk second phases are broken and dispersed in the matrix, but also new second phases will be precipitated, which strengthens the matrix and grain boundaries. Therefore, the elevated temperature strength of the alloy can be improved with the increase of Al content. However, a large number of second phases will form in the alloys and aggregate at the grain boundaries when the Al content is excessive, thereby reducing elevated temperature strength of the alloys.

Figures 14 and 15 show the tensile fracture morphology of the as-extruded ZTM641 and ZTM641–2Al alloys at 150 and 200 °C, respectively. From the SE-SEM images, it can be

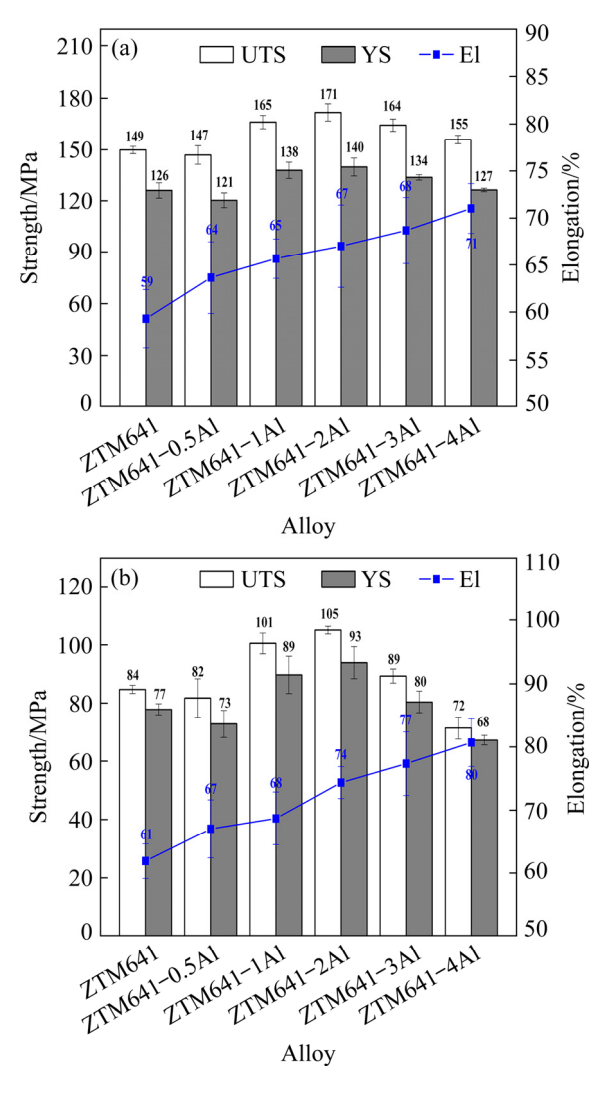


Fig. 13 Mechanical properties of as-extruded ZTM641–xAl tested at 150 °C (a) and 200 °C (b)

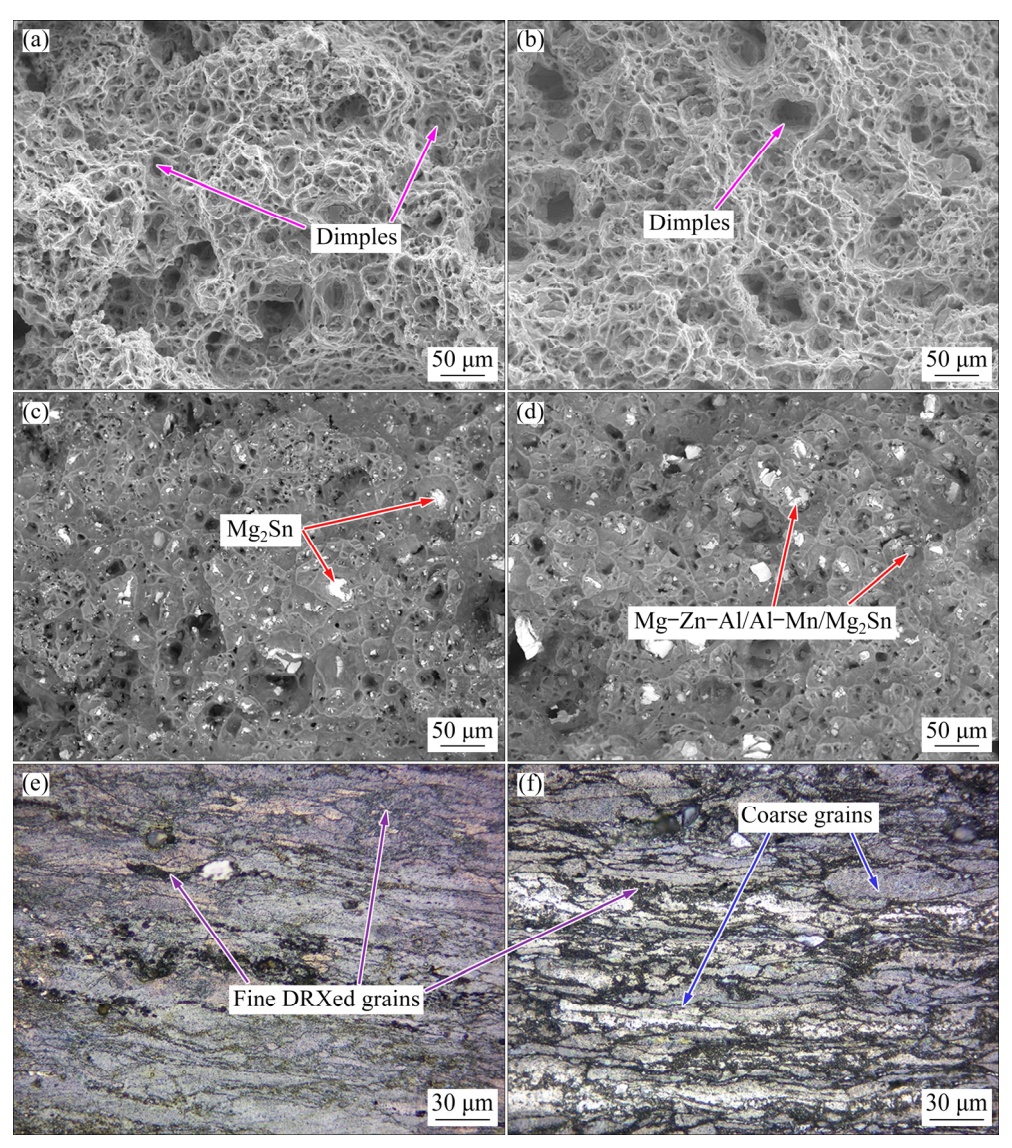


Fig. 14 SE-SEM (a, b) and BSE-SEM (c, d) micrographs of fracture surface, and optical images from longitudinal sections adjacent to fracture surface (e, f) of as-extruded ZTM641-xAl alloy at 150 °C: (a, c, e) x=0; (b, d, f) x=2

that the fracture morphology seen experimental alloys is dominated by dimples, mainly ductile fracture. It can be seen from the BSE-SEM images that compared with the fracture at RT, the bulk second phases on the hightemperature fracture surface is significantly reduced, and the dispersed second phase is increased, so the temperature elongation is Comparing ZTM641 and ZTM641-2Al alloys, the Al addition increases the volume fraction of fine particle phases and the elevated temperature strength. From the metallographic images of the longitudinal section of the fracture, it can be seen that the microstructure transforms into large grains and many fine DRXed grains are generated when tested at 150 °C, indicating that the contribution of

DRX plays an important role in elevated temperature mechanical properties. When the temperature is increased to 200 °C, the finer second phases are dispersed in the matrix and effectively inhibit the grain growth during the DRX. Compared with 150 °C, the grains are finer and more uniform after the 200 °C tensile test, which can be proved from Fig. 16.

Compared with the RT properties, the elevated temperature strength of the experimental alloys decreases and the elongation increases. On one hand, as the temperature increases, the storage energy of the matrix increases and the incubation period of DRX decreases, making it difficult to produce the effect of work hardening. On the other hand, higher deformation temperature improves the

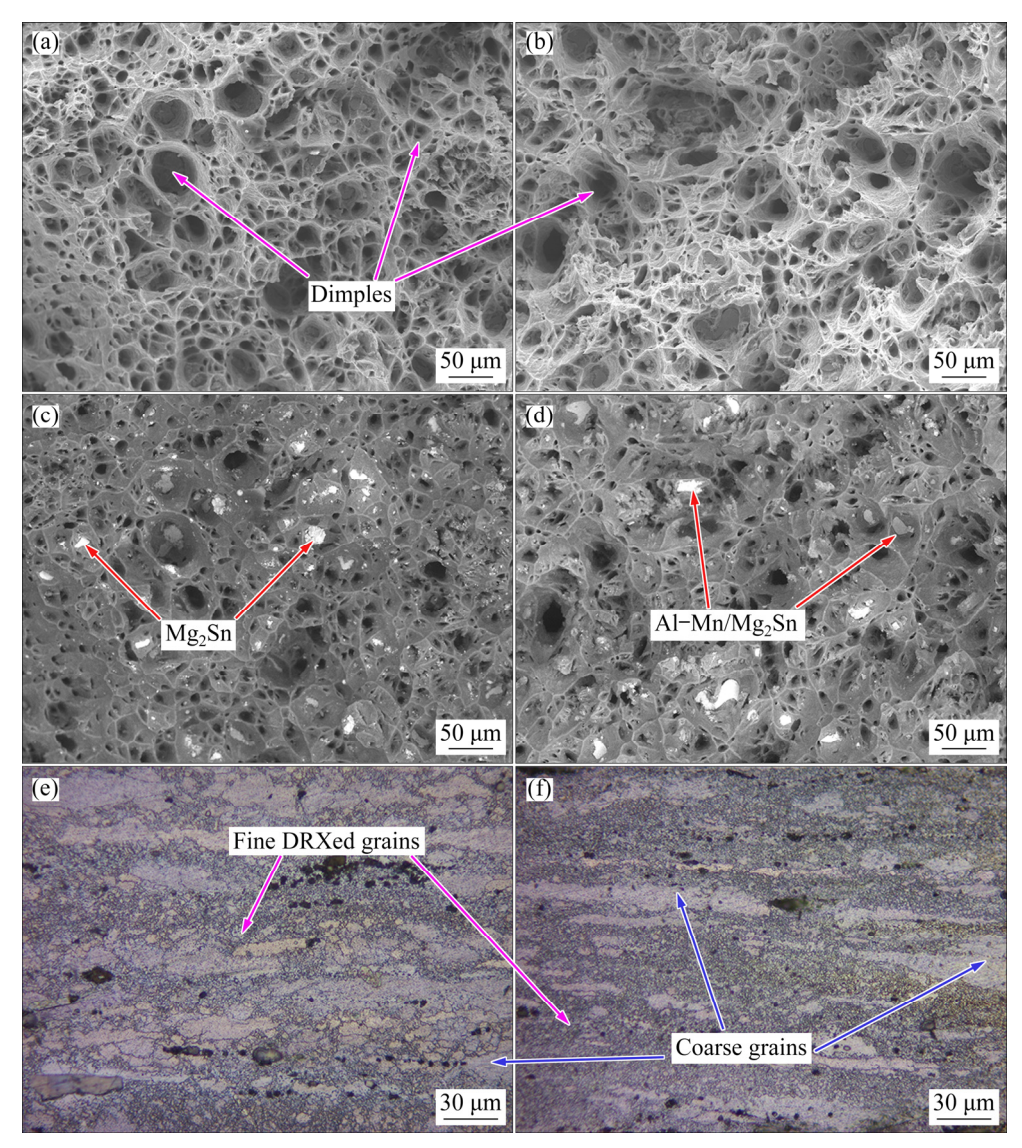


Fig. 15 SE-SEM (a, b) and BSE-SEM (c, d) micrographs of fracture surface, and optical images from longitudinal sections adjacent to fracture surface (e, f) of as-extruded ZTM641-xAl alloy at 200 °C: (a, c, e) x=0; (b, d, f) x=2

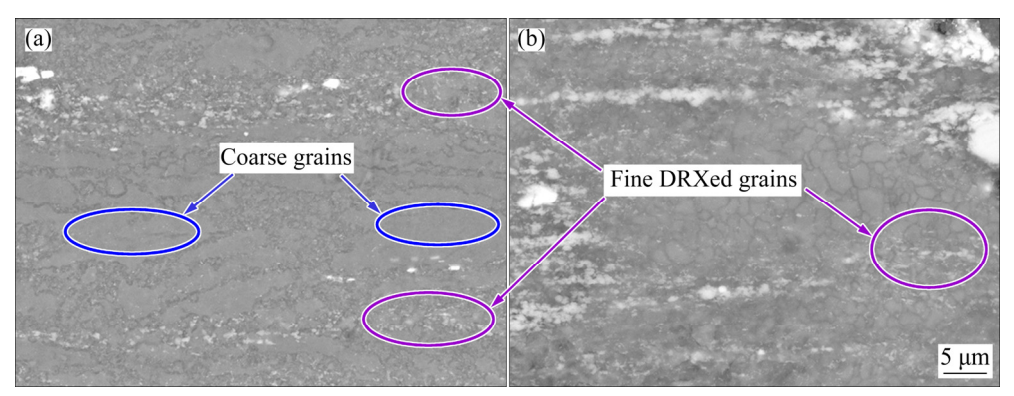


Fig. 16 BSE-SEM images from longitudinal sections adjacent to fracture surface of as-extruded ZTM641–4Al alloy at $150 \,^{\circ}$ C (a) and $200 \,^{\circ}$ C (b)

mobility of the grain boundaries, which can reduce the stress concentration caused by the inhomogeneous deformation [48]. Compared with RT, during the elevated temperature tensile, due to the enhancement of atomic thermal vibration and the increase of the diffusion rate, the grain boundary migration ability of the experimental alloy is enhanced, resulting in an increase in the nucleation rate of DRX and promoting DRX. The DRX causes the transformation of the sub-grain boundary from a small angle grain boundary to a high angle grain boundary, which is beneficial to consuming a large number of dislocations and leading to finer original structure. Besides, higher solute atom content and few dislocations tested at 150 and 200 °C will also improve the coordinate deformation. Therefore, although the elevated temperature strength of the alloy is reduced, the high temperature elongation is significantly improved.

4 Conclusions

- (1) The as-cast ZTM641 alloy is mainly composed of α -Mg, α -Mn, Mg₂Sn and Mg₇Zn₃ eutectic phases. The Al addition results in the formation of Al₈Mn₅, Al₁₁Mn₄, Mg₃₂(Al,Zn)₄₉, Al₂Mg₅Zn₂ and MgZn phases.
- (2) The as-extruded experimental alloys exhibit a mixed crystal structure with DRXed fine grains. A small amount of Al (\leq 1%) can effectively refine the dendrites and increase the proportion of DRXed fine grains during hot extrusion process. A high content of Al (\geq 2%) forms a variety of large secondary phases, fine secondary phases decrease, and grain size increases.
- (3) A small amount of Al can improve the RT mechanical properties of the as-extruded ZTM641 alloy, which is due to the second phase dispersion distribution and DRXed fine grains. The Al addition can improve the elevated temperature properties of the as-extruded ZTM641 alloy. Among them, ZTM641–2Al alloy has the highest strength, which is mainly due to the formation of thermally stable phases, such as Al₈Mn₅, Mg₂Sn and Mg₃₂(Al,Zn)₄₉. In addition, after the 4% Al addition, the elongations at 150 and 200 °C of the as-extruded alloys are as high as 71% and 80%.

Acknowledgments

The authors are grateful for the financial supports from the National Natural Science Foundation of China (No. 51701172), Educational Commission of Hunan Province, China (No. 20B579), Major Program of Hunan Province, China (No. 2018RS3091), China Postdoctoral

Science Foundation (No. 2018M632977), and the Natural Science Foundation of Hunan Province, China (No. 2018JJ3504).

References

- [1] ZHU S Q, YANG H G, LIAO X Z, MOODY S, SHA G, WU Y Z, RINGER S P. Mechanisms for enhanced plasticity in magnesium alloys [J]. Acta Materialia, 2015, 82: 344–355.
- [2] GUO Li-li, FUJITA F. Influence of rolling parameters on dynamically recrystallized microstructures in AZ31 magnesium alloy sheets [J]. Journal of Magnesium and Alloys, 2015, 3(2): 95–105.
- [3] ZHANG Wan-peng, MA Ming-long, YUAN Jia-wei, SHI Guo-liang, LI Yong-jun, LI Xing-gang, ZHANG Kui. Microstructure and thermophysical properties of Mg-2Zn-xCu alloys [J]. Transactions of Nonferrous Metals Society of China, 2020, 30(7): 1803–1815.
- [4] YU Wen-hua, WANG Huan-lei, LIU Shuang, MAO Nan, LIU Xiao, SHI Jing, LIU Wei, CHEN Shou-gang, WANG Xin. N, O-codoped hierarchical porous carbons derived from algae for high-capacity supercapacitors and battery anodes [J]. Journal of Materials Chemistry, 2016, 4(16): 5973–5983.
- [5] GAO Lei, YAN Hong, LUO Jun, LUO A A, CHEN Rong-shi. Microstructure and mechanical properties of a high ductility Mg–Zn–Mn–Ce magnesium alloy [J]. Journal of Magnesium and Alloys, 2013, 1(4): 283–291.
- [6] CHENG Yuan-fen, DU Wen-bo, LIU Ke, FU Jun-jian, WANG Zhao-hui, LI Shu-bo, FU Jin-long. Mechanical properties and corrosion behaviors of Mg-4Zn-0.2Mn-0.2Ca alloy after long term in vitro degradation [J]. Transactions of Nonferrous Metals Society of China, 2020, 30(2): 363-372.
- [7] DONG Xu-guang, FU Jun-wei, WANG Jing, YANG Yuan-sheng. Microstructure and tensile properties of as-cast and as-aged Mg-6Al-4Zn alloys with Sn addition [J]. Materials & Design, 2009, 51: 567-574.
- [8] OHISHI K, HONO K, SHIN K S. Effect of pre-aging and Al addition on age-hardening and microstructure in Mg-6wt%Zn alloys [J]. Materials Science and Engineering A, 2008, 496(1-2): 425-433.
- [9] WANG Yong-jian, PENG Jian, ZHONG Li-ping. On the microstructure and mechanical property of as-extruded Mg-Sn-Zn alloy with Cu addition [J]. Journal of Alloys and Compounds, 2018, 744: 234-242.
- [10] MENDIS C L, OHISHI K, OHKUBO T, SHIN K S, HONO K. Microstructures and mechanical properties of extruded and heat treated Mg–6Zn–1Si–0.5Mn alloys [J]. Materials Science and Engineering A, 2012, 533: 1–9.
- [11] LEE Y C, DAHLE A K, STJOHN D H. The role of solute in grain refinement of magnesium [J]. Metallurgical and Materials Transactions A, 2000, 31(11): 2895–2906.
- [12] BANBERGER M. Structural refinement of cast magnesium alloys [J]. Materials Science and Technology, 2001, 17(1): 15–24.
- [13] SASAKI T T, OHISHI K, OHKUBO T, HONO K. Enhanced age hardening response by the addition of Zn in Mg–Sn alloys [J]. Scripta Materialia, 2006, 55(3): 251–254.

- [14] HU Guang-shan, ZHANG Ding-fei, TANG Tian, JIANG Lu-yao, PAN Fu-sheng. Effect of extrusion temperatures on microstructures and mechanical properties of Mg-6Zn-1Mn-4Sn-0.5Y alloy [J]. Rare Metal Materials and Engineering, 2016, 45(5): 1111-1116.
- [15] GORNY A, BANBERGER M, KATSMAN A. High temperature phase stabilized microstructure in Mg–Zn–Sn alloys with Y and Sb additions [J]. Journal of Materials Science, 2007, 42(24): 10014–10022.
- [16] HU Guang-shan, ZHANG Ding-fei, ZHAO Ding-zang, SHEN Xia, JIANG Lu-yao, PAN Fu-sheng. Microstructures and mechanical properties of extruded and aged Mg-Zn-Mn-Sn-Y alloys [J]. Transactions of Nonferrous Metals Society of China, 2014, 24(10): 3070-3075.
- [17] HOU Li-da, LI Zhen, ZHAO Hong, PAN Yu, PAVLINICH S, LIU Xi-wei, LI Xi-lin, ZHENG Yu-feng, LI Li. Microstructure, mechanical properties, corrosion behavior and biocompatibility of as-extruded biodegradable Mg-3Sn-1Zn-0.5Mn alloy [J]. Journal of Materials Science & Technology, 2016, 32(9): 874-882.
- [18] HOU Cai-hong, QI Fu-gang, YE Zhi-song, ZHAO Nie, ZHANG Ding-fei, OUYANG Xiao-ping. Effects of Mn addition on the microstructure and mechanical properties of Mg–Zn–Sn alloys [J]. Materials Science and Engineering A, 2020, 774: 138933.
- [19] LIU Qiang, CHENG Wei-li, ZHANG Hui, XU Chun-xiang, ZHANG Jin-shan. The role of Ca on the microstructure and corrosion behavior of Mg–8Sn–1Al–1Zn–Ca alloys [J]. Journal of Alloys and Compounds, 2014, 590: 162–167.
- [20] WANG Bo, PAN Fu-sheng, CHEN Xian-hua, GUO Wei, MAO Jian-jun. Microstructure and mechanical properties of as-extruded Mg-Sn-Al-Zn alloys [J]. Materials Science and Engineering A, 2012, 656: 165-173.
- [21] KANG D H, PARK S S, KIM N J. Development of creep resistant die cast Mg-Sn-Al-Si alloy [J]. Materials Science and Engineering A, 2005, 413: 555-560.
- [22] SHE Jia, PAN Fu-sheng, HU Huan-huan, PAN Hu-cheng, TANG Ai-tao, SONG Kai, YU Zheng-wen, LUO Su-qin. Microstructures and mechanical properties of as-extruded Mg-5Sn-1Zn-xAl (x=1, 3 and 5) alloys [J]. Progress in Natural Science: Materials International, 2015, 25(4): 267–275.
- [23] KIM S, LEE J U, KIM Y J, JUNG J, PARK S H. Controlling the microstructure and improving the tensile properties of extruded Mg–Sn–Zn alloy through Al addition [J]. Journal of Alloys and Compounds, 2018, 751: 1–11.
- [24] GU Dong-dong, WANG Jia-wen, CHEN Yu-bin, PENG Jian. Effect of Mn addition and refining process on Fe reduction of Mg-Mn alloys made from magnesium scrap [J]. Transactions of Nonferrous Metals Society of China, 2020, 30(11): 2941–2951.
- [25] SHI Guo-liang, ZHANG Ding-fei, ZHAO Xia-bing, ZHANG Kui, LI Xing-gang, LI Yong-jun, MA Ming-long. Precipitate evolution in Mg-6wt.%Zn-1wt.%Mn alloy [J]. Rare Metal Materials and Engineering, 2013, 42(12): 2447–2452.
- [26] YU Zheng-wen, HU Meng-die, TANG Ai-tao, WU Ming-song, HE Jie-jun, GAO Zheng-yuan, WANG Fang-yuan, LI Cai-yu, CHEN Bin, LIU Jian-guo. Effect of

- aluminium on the microstructure and mechanical properties of as-cast magnesium-manganese alloys [J]. Materials Science and Technology, 2017, 33(17): 2086–2096.
- [27] QI Fu-gang, ZHANG Ding-fei, ZHANG Xiao-hua, XU Xing-xing. Effect of Sn addition on the microstructure and mechanical properties of Mg–6Zn–1Mn (wt.%) alloy [J]. Journal of Alloys and Compounds, 2014, 585: 656–666.
- [28] EASTON M A, STJOHN D H. A model of grain refinement incorporating alloy constitution and potency of heterogeneous nucleant particles [J]. Acta Materialia, 2001, 49(10): 1867–1878.
- [29] LEE Y C, DAHLE A K, STJOHN D H. The role of solute in grain refinement of magnesium [J]. Metallurgical and Materials Transactions A, 2000, 31(11): 2895–2906.
- [30] FU J W, YANG Y S, Formation of the solidified microstructure in Mg–Sn binary alloy [J]. Journal of Crystal Growth, 2011, 322(1): 84–90.
- [31] GAO X, NIE J F. Structure and thermal stability of primary intermetallic particles in an Mg–Zn casting alloy [J]. Scripta Materialia, 2007, 57(7): 655–658.
- [32] CELOTTO S, BASTOW T J. Study of precipitation in aged binary Mg-Al and ternary Mg-Al-Zn alloys using 27Al NMR spectroscopy [J]. Acta Materialia, 2001, 49(1): 41-51.
- [33] ZHANG Jin-shan, ZHANG Yong-qing, ZHANG Yan, XU Chun-xiang, WANG Xiao-ming, YAN Jie. Effect of Mg-based spherical quasicrystal on microstructures and mechanical properties of ZA54 alloy [J]. Transactions of Nonferrous Metals Society of China, 2010, 20(7): 1199–1204.
- [34] SHE J, PAN Fu-sheng, ZHANG Jian-yue, TANG Ai-tao, LUO S, YU Z, SONG Kai, RASHAD M. Microstructure and mechanical properties of Mg-Al-Sn extruded alloys [J]. Journal of Alloys and Compounds, 2015, 657: 893–905.
- [35] BAMBERGUR M. Phase formation in Mg-Sn-Zn alloys— Thermodynamic calculations vs experimental verification [J]. Journal of Materials Science, 2006, 41(10): 2821–2829.
- [36] SHUKLA A, PELTON A D. Thermodynamic assessment of the Al–Mn and Mg–Al–Mn systems [J]. Journal of Phase Equilibria and Diffusion, 2009, 30(1): 28–39.
- [37] HAITANI T, TAMURA Y, MOTEGI T, KONO N, TAMEHIRO H. Solubility of iron in pure magnesium and cast structure of Mg-Fe alloy [J]. Materials Science Forum, 2006, 419–422: 697–702.
- [38] OHNO M, MIRKOVIC D, SCHMIDFETZER R. Liquidus and solidus temperatures of Mg-rich Mg-Al-Mn-Zn alloys [J]. Acta Materialia, 2006, 54(15): 3883-3891.
- [39] YANG Ming-bo, PAN Fu-sheng, LI Zhong-sheng, SHEN Jia. Effect of mass ratio of Zn to Al on as-cast microstructure and solidification behaviour of Mg–Zn–Al ternary magnesium alloys [J]. The Chinese Journal of Nonferrous Metals, 2008, 18(7): 1191–1198. (in Chinese)
- [40] ZHANG Zhan, COUTURE A, LUO A A. An investigation of the properties of Mg–Zn–Al alloys [J]. Scripta Materialia, 1998, 39(1): 45–53.
- [41] LUO A A, ZHANG C, SACHDEV A K. Effect of eutectic temperature on the extrudability of magnesium–aluminum alloys [J]. Scripta Materialia, 2012, 66(7): 491–494.
- [42] STJOHN D H, QIAN M, EASTON M A, CAO P. The

- interdependence theory: The relationship between grain formation and nucleant selection [J]. Acta Materialia, 2011, 59(12): 4907–4921.
- [43] HUMPHREYS J F. Nucleation in recrystallization [J]. Materials Science Forum, 2004, 467–470: 107–116.
- [44] SASAKI T T. OHISHI K, OHKUBO T, HONO K. Effect of double aging and microalloying on the age hardening behavior of a Mg–Sn–Zn alloy [J]. Materials Science and Engineering A, 2011, 530: 1–8.
- [45] SHI Z Z, ZHANG W Z. Investigation on the microstructure of a τ-Mg₃₂(Al, Zn)₄₉ strengthened Mg–Zn–Al alloy with relatively low Zn content [J]. Phase Transitions, 2012,

- 85(1-2): 41-51.
- [46] WANG Y, XIA M, FAN Z, ZHOU X, THOMPSON G E. The effect of Al₈Mn₅ intermetallic particles on grain size of as-cast Mg-Al-Zn AZ91D alloy [J]. Intermetallics, 2010, 18(8): 1683-1689.
- [47] MA Yan-long, PAN Fu-sheng, ZUO Ru-lin. Review on the research of high-strength wrought magnesium alloy ZK60 [J]. Journal of Chongqing University, 2004, 27(9): 80–86. (in Chinese)
- [48] MA Z Y, TJONG S C. Creep deformation characteristics of discontinuously reinforced aluminium-matrix composites [J]. Composites Science and Technology, 2001, 61(5): 771–786.

Al 添加对 Mg-Zn-Sn-Mn 合金 显微组织和力学性能的影响

侯彩红 1,2 , 叶芝松 1,2 , 齐福刚 1,2 , 汪 清 3 , 李连辉 1,2 , 欧阳晓平 1,2 , 赵 镍 1,2

- 1. 湘潭大学 材料科学与工程学院,湘潭 411105;
- 2. 湘潭大学 低维材料与应用技术教育部重点实验室,湘潭 411105;
 - 3. 中铁二院工程集团有限公司,成都 610000

摘 要:通过光学显微镜(OM)、X 射线衍射仪(XRD)、差示扫描量热仪(DSC)、扫描电子显微镜(SEM)、透射电子显微镜(TEM)和单轴拉伸试验,研究不同 Al 含量(0、0.5、1、2、3 和 4,质量分数,%)对铸态、均匀化态和挤压态 Mg-6Zn-4Sn-1Mn(ZTM641)合金显微组织和力学性能的影响。结果表明: 当 Al 含量不高于 0.5%时,合金主要由 α -Mg、Mg₂Sn、Al₈Mn₅和 Mg₇Zn₃相组成; 当 Al 含量高于 0.5%时,合金主要由 α -Mg、Mg₂Sn、MgZn、Mg₃₂(Al,Zn)₄₉、Al₂Mg₅Zn₂、Al₁₁Mn₄和 Al₈Mn₅相组成; 少量的 Al(\leq 1%)可以增加热挤压过程中动态再结晶细小晶粒的比例。在室温拉伸试验条件下,ZTM641-1Al 合金具有最佳的综合力学性能,其极限抗拉强度为 332 MPa,屈服强度为 221 MPa,伸长率为 15%;在 150 和 200 °C 高温拉伸试验条件下,ZTM641-2Al 合金具有最佳的综合力学性能。

关键词: Mg-Zn-Sn-Mn 合金; Al; 显微组织; 力学性能; 动态再结晶; 形核

(Edited by Xiang-qun LI)